Compression and spallation properties of polyethylene terephthalate under plate impact loading

Y.L. Bian [a], H.W. Chai [b], S.J. Ye [c], H.L. Xie [d], X.H. Yao [a,**], Y. Cai [b,*]

[a] Department of Engineering Mechanics, South China University of Technology, Guangzhou, Guangdong 510640, PR China
[b] The Peac Institute of Multiscale Sciences, Chengdu, Sichuan 610031, PR China
[c] School of Materials Science and Engineering, Southwest Jiaotong University, Chengdu, Sichuan 610031, PR China
[d] Shanghai Institute of Applied Physics, Chinese Academy of Sciences, Shanghai 201204, PR China

ABSTRACT

We conduct plate impact experiments to investigate shock compression and spallation properties of polyethylene terephthalate. The Hugoniot equation of state, the apparent velocity–particle velocity relation, and the indices of refraction are obtained from Hugoniot experiments. Spall strength, as well as tensile strain rate is deduced at shock pressures up to ~2.4 GPa in spallation shots. At low shock pressures (<0.6 GPa), the spall strength increases slightly with increasing shock pressure, as a result of increasing tensile strain rate. Release melting is observed at high impact velocities (>816 m s^{-1}). Via X-ray computed tomography, three-dimensional void and crack structures are revealed for shock-recovered specimens. Small voids appear thin and curved for low-speed impacts but become ellipsoidal for high-speed impacts. Such different void shapes may be attributed to the diverse damage mechanisms at different impact velocities.

1. Introduction

Polyethylene terephthalate (PET), a semicrystalline thermoplastic polyester, is an engineering material often used as transparent elements in dynamic protective equipment given the combination of good optical transparency, and reasonable thermal stability and tensile strength [1–3]. After being modified by blending with other polymers, PET exhibits excellent tensile and impact properties, and has been widely used in automobile industries, machinery fields and artificial ligaments [4,5]. Its tensile (spall fracture) and compressive (equation of state, EOS) properties under dynamic loading are of particular interest for such applications.

Previous experiments were mostly under intermediate and low strain rates. Martinez et al. [6] conducted drop-weight tests on a modified type of PET and established a nonconservative model to evaluate the elastic modulus under low-strain-rate loadings. Bai et al. [3] employed a drop-weight impact system and a universal testing machine to investigate the strain rate effect on the dynamic tensile properties of the PET fiber bundle (from 1/600 to 160 s^{-1}). With increasing strain rate, its elastic modulus and tensile strength increase, whereas its toughness and failure strain decrease. Bragov and Lomunov [7] conducted split

Hopkinson pressure bar (SHPB) tests on PET at strain rates from 5×10^2 to 3×10^3 s^{-1}, and observed an increase in Young's modulus and fracture stress with increasing strain rate. However, dynamic properties of PET under higher strain rate impact loading, including the spall strength and Hugoniot EOS, are rarely studied.

Besides mechanical properties, the spallation or damage mechanisms of PET at the microscopic level are also interesting due to its potential applications as an engineering material. Most previous studies along this line used scanning electron microscopy for two-dimensional (2D) analysis of postmortem samples [8,9]. Curran et al. conducted 2D analysis on polycarbonate (PC) under plate impact loading, and revealed the damage mechanisms: crack nucleation, growth, and coalescence [10]. As technology advances, X-ray computed tomography (CT) can be exploited to characterize three-dimensional (3D) microstructure in various materials [11–16]. Compared to 2D information, 3D microstructure is able to provide more details regarding the evolution process of damage at the microscopic level. Verker et al. [17] examined the internal structure of a polymide film recovered from laser-driven flyer experiments with CT, and the crack configurations indicate a ductile to brittle transition in spall failure as impact velocity increases. In another study

---

with plate impact loading, postmortem PC was characterized with CT, and different damage mechanisms were deduced at different impact velocities [18].

Polymers such as polymethyl methacrylate (PMMA) [19,20] and PC [21] can be used as optical window in shockwave experiments for their transparency under shock loading. The refractive index and Hugoniot EOS of a window material can be determined simultaneously [22]. PET is a potential low-impedance window material for shock experiments. However, its Hugoniot equation of state, index of refraction, and transparency under shock loading are unknown.

In this work, we adopt plate impact experiments to investigate the spallation and shock-compression properties of PET. Its Hugoniot EOS is measured up to ∼2.4 GPa (real particle velocity of 543 m s^{-1}). We obtain the indices of refraction at different shock states with a multi-channel laser Doppler velocimeter. Free surface velocity time histories are obtained up to ∼1100 m s^{-1} (corresponding to a peak shock stress of 2.4 GPa) for spallation experiments, from which tensile strain rates and spall strengths are derived. Release melting is revealed from free surface velocity histories at different impact velocities. The recovered specimens are then examined with CT to map 3D void structures. Small voids differ remarkably in shape between high- and low-speed shots, due to the different mechanisms of spallation damage (possibly, interchain fracture versus intrachain breakage).

2. Principle and interpretation of the experiment

Commercially available PET is chosen as the experimental material. The bulk density under ambient conditions, $\rho_0 = 1.34$ g cm^{-3}, is obtained via the Archimedean method. With an ultrasonic device (5073PR, Olympus), its transverse and longitudinal sound speeds are measured to be 0.972 and 2.322 km s^{-1}, respectively. The index of refraction at 1550 nm wavelength measured by an Abbe refractometer, is $n_0 = 1.5476$, similar to the literature value [23]. The Poisson's ratio, ν, is calculated to be 0.394.

A single-stage gas gun is used to conduct plate impact experiments. The bore diameter of the gun is 14 mm. Figure 1(a) and (b) present the schematic setups of the spallation and Hugoniot experiments, respectively. For the two types of experiments, a recess (3) is machined at one end of a sabot (1), and a flyer plate (2) is then attached to this end. Polycarbonate, Al and Cu sabots are used for different launching velocities, and two O-rings (4) are fixed to the sabot to avoid leakage of gas. High pressure gas (helium or nitrogen) is released into the gun barrel (5) when the gun is fired, to accelerate the sabot and flyer to impact the PET sample (6). In spallation experiments, the impact velocity (u_{imp}) is measured through an optical beam blocking (OBB) system (7) with an accuracy of 0.5% when the sabot exits the muzzle [24,25].

For Hugoniot experiments, a thin silver film (9) is used to reflect the probe light on part of the impact surface of a target. As shown in
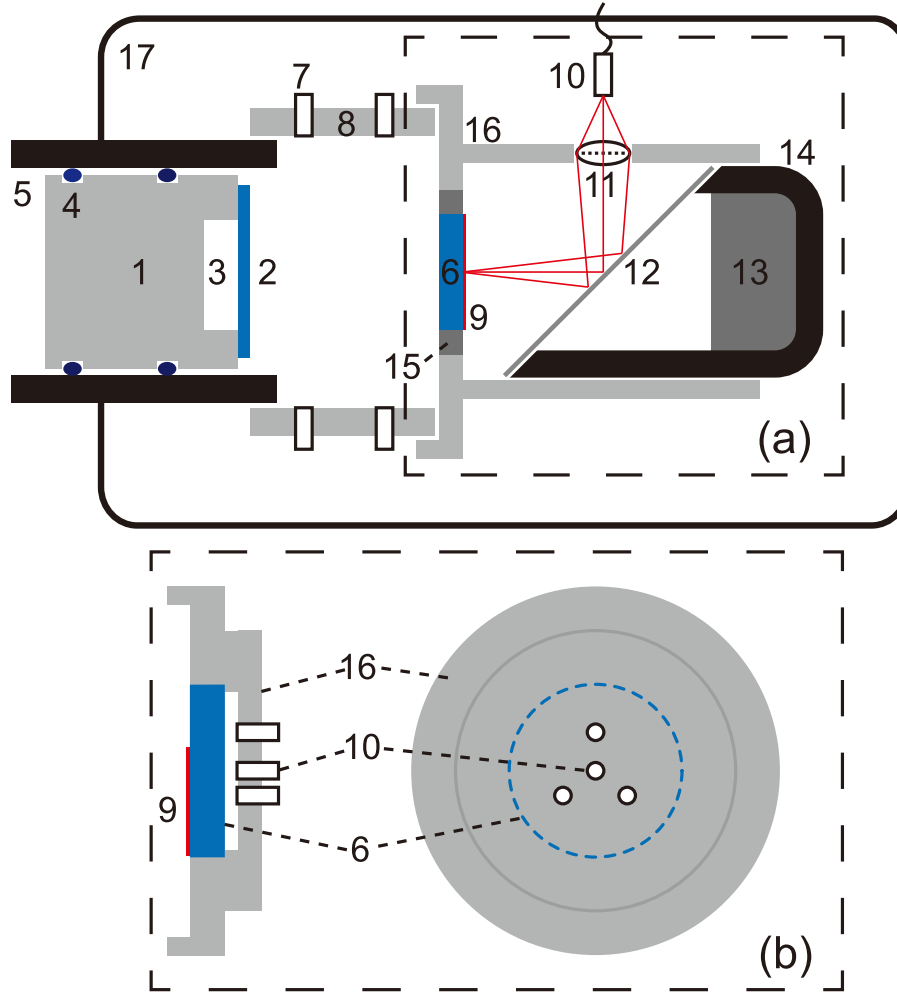

Fig. 1. Schematic setups for plate impact experiments: (a) spallation experiments and (b) Hugoniot experiments. 1: sabot; 2: flyer plate; 3: recess; 4: O-ring; 5: gun barrel; 6: sample; 7: optical fibers for the optical beam block system; 8: fiber holder; 9: Ag coating for reflecting probe light; 10: optical fibers for the Doppler pin system; 11: optical lens; 12: reflecting mirror; 13: soft recovery materials; 14: recovery cylinder; 15: momentum trap; 16: sample holder; 17: vacuum chamber.

Ref. [26], a four-channel Doppler pin system (DPS) is adopted to obtain u_{imp} and capture the shock breakouts at the impact surface and the target free surface. For each channel, a single-mode optical fiber (10) is attached with a ceramic pin (flat-ended ferrule with $\sim 2.5\%$ efficiency of retro-reflection, 1.25 mm diameter), and is then used as the optical probe. A single-frequency (wavelength $\lambda = 1550$ nm) fiber laser is utilized as the probe laser. Each optical probe is connected to a DPS detector, and all four probes are placed about 0.6 mm to rear surface of the sample.

The sample rear surface is entirely coated by a silver layer to reflect the probe light for spallation experiments. A single-channel DPS is used together with a lens (11) and a reflecting mirror (12) to measure the free surface velocity (u_{fs}) history of the sample. Using soft materials (13), the targets are "soft-recovered" after impact for CT characterization. In spallation experiments, a well-designed momentum trapping ring (15) assembly is adopted to mitigate radial release waves [27,28].

For symmetric impact, samples and flyer plates are both PET. We polish the front and rear surfaces of the sample and flyer plate to mirror finish or micron level for better impact and reflection efficiency. The diameters of targets and flyers are both 13.2 mm for Hugoniot experiments, while their thicknesses are 1.9 mm and 2.9 mm, respectively. Three optic fibers for DPS are uniformly distributed around the central probe with a diameter of 6 mm [Fig. 1(b)]. In spallation experiments, the flyer thickness and diameter are 0.9 mm and 13.2 mm, respectively, for the convenience of recovery. We set the diameter of target as 9 mm to prevent the flyer and sabot passing through the sample holder (16). Thickness of the target is set as 1.9 mm to avoid edge release.

The postmortem specimens are analyzed with CT to quantify the characteristics of cracks and voids [29,30]. As a nondestructive 3D technique, CT can be used to resolve internal microstructures of samples. The white beam X-ray propagates through the sample after filtering by a 2 mm thick Al. A charge coupled device (CCD) camera is used to record the transmission signal with a $10\times$ lens array. The exposure time is 0.66 ms and the field of view is 1.925×1.925 mm^2. 1250 projections are collected within $0° - 180°$ for each tomography scan, which are then reconstructed into 3D micrographs with an open-source software, *TomoPy* [31].

3. Results and discussion

3.1. Hugoniot experiments

A typical DPS fringe pattern of shot MP660 is shown in Fig. 2. The signal is measured from the central probe, and time zero is shifted to stand for the entry time of shock wave into the sample. The velocity of shock wave, i.e., shock velocity (u_s), can be determined from the sample thickness (h_s) and shock transit time (t_1) via $u_s = h_s / t_1$. Here t_1 is the propagation time of shock wave in the sample determined from the voltage–time output of the oscilloscope [Fig. 2(a)]. For each shot, u_s is the average signal over four DPS channels. For symmetric impact loading, the u_{imp} on the shock plateau (u_p) is essentially half of u_{imp}, i.e., $u_p = \frac{1}{2}u_{imp}$. For the single-wave structure, the peak shock stress and strain are obtained as $\sigma_H = \rho_0 u_s u_p$ and $\varepsilon = u_p/u_s$, respectively.

We carry out 11 Hugoniot shots on PET, and Table 1 shows the relevant parameters and results. The compressive yield strength of polycarbonate is very low, so the elastic shock speed is close to the initial longitudinal sound velocity (2.322 km s^{-1}). Even for a low-speed shot ($u_{imp} = 97$ m s^{-1}), the plastic shock speed (2.501 km s^{-1}) is higher than the elastic shock speed, i.e., the elastic precursor is overtaken by the plastic shock, so HEL is not detected in our experiments. The $u_s - u_p$ relation is also depicted in Fig. 3. u_s increases linearly with u_p at high u_p (>250 m s^{-1}), while a hump appears at low u_p (<250 m s^{-1}). This anomalous behavior at low u_p is quite common for other polymers like PMMA [19], polyethylene (PE) [32], estane [33] and polyvinylidene fluoride (PVDF) [34]. Barker and Hollenbach [19] inferred that the
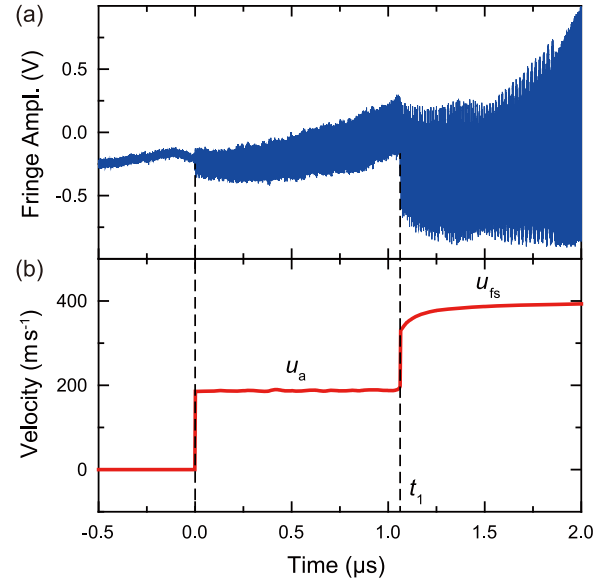

Fig. 2. DPS measurement from the central probe: (a) Fringe pattern from oscilloscope and (b) corresponding velocity history for shot MP660. Time zero is shifted to shock entry into the target, and t_1 is the shock arrival time at the target free surface. u_a: apparent velocity; u_{fs}: free surface velocity.

Table 1
Experimental data and parameters for the Hugoniot experiments. h_s: sample thickness; h_f: flyer plate thickness; u_p: shock-state particle velocity; u_{imp}: impact velocity; u_a: apparent velocity; u_s: shock velocity; n_H: shock-state refractive index; σ_H: peak stress; ρ: density at shock state. The uncertainties is indicated by the numbers in the parentheses for the last one or two digits.

| Shot number	h_s (mm)	h_f (mm)	u_p (km s^{-1})	u_{imp} (km s^{-1})	u_a (km s^{-1})	u_s (km s^{-1})	n_H	σ_H (GPa)	ρ (g cm^{-3})
MP651	2.925 (2)	1.897 (2)	0.048 (1)	0.097 (1)	0.045 (1)	2.501 (9)	1.5597 (7)	0.161 (3)	1.3613 (7)
MP657	2.950 (2)	1.901 (2)	0.097 (1)	0.195 (1)	0.091 (2)	2.606 (19)	1.5716 (10)	0.339 (4)	1.3868 (8)
MP658	2.932 (2)	1.922 (2)	0.154 (1)	0.309 (2)	0.145 (2)	2.707 (4)	1.5844 (8)	0.558 (4)	1.4158 (5)
MP660	2.957 (2)	1.906 (2)	0.200 (1)	0.399 (2)	0.187 (1)	2.787 (4)	1.5946 (8)	0.742 (5)	1.4379 (7)
MP653	2.934 (2)	1.909 (2)	0.268 (1)	0.536 (3)	0.249 (1)	2.857 (9)	1.6116 (10)	1.022 (7)	1.4731 (11)
MP664	2.946 (2)	1.896 (2)	0.310 (2)	0.619 (3)	0.291 (2)	2.907 (18)	1.6199 (13)	1.202 (11)	1.4942 (17)
MP669	2.925 (2)	1.898 (2)	0.354 (2)	0.708 (4)	0.335 (9)	2.987 (16)	1.6285 (35)	1.411 (12)	1.5144 (17)
MP655	2.929 (2)	1.920 (2)	0.402 (2)	0.804 (4)	0.374 (3)	3.052 (23)	1.6413 (18)	1.638 (16)	1.5375 (25)
MP671	2.931 (2)	1.894 (2)	0.456 (2)	0.912 (5)	0.424 (1)	3.120 (19)	1.6534 (18)	1.900 (17)	1.5635 (24)
MP672	2.943 (2)	1.893 (2)	0.502 (3)	1.005 (5)	0.468 (1)	3.181 (43)	1.6633 (25)	2.133 (32)	1.5854 (50)
MP675	2.927 (2)	1.893 (2)	0.543 (3)	1.087 (5)	0.505 (7)	3.256 (29)	1.6714 (33)	2.362 (26)	1.6025 (38)
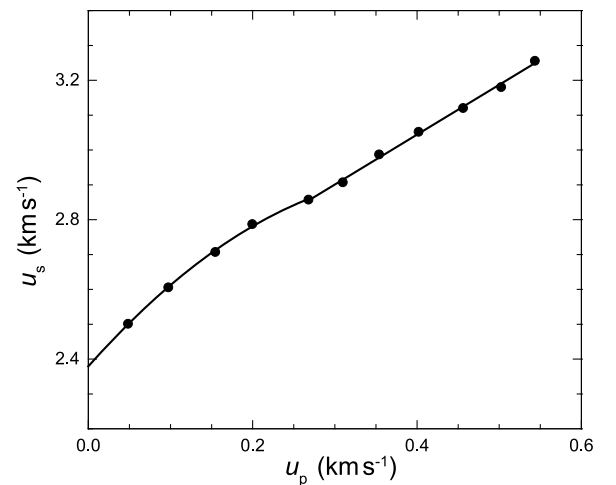
Fig. 3. $u_s - u_p$ plot of PET. The solid curve and line denote the quadratic fitting for $u_p < 250$ m s^{-1} and the linear fitting for $u_p > 250$ m s^{-1}, respectively.

hump in PMMA is caused by plastic yielding. Bourne and Millett [35] attributed the kink in PMMA to the influence of electronic interactions between the packed polymer chains and van de Waals interactions between intermolecular atoms. The kink of PET in $u_s - u_p$ relation may also due to these two reasons. We use quadratic $u_s = C_0 + s_1 u_p + s_2 u_p^2$ and linear $u_s = C_0 + su_p$ fittings (both in km s^{-1}) for the low and high u_p regimes, respectively (the solid curve and line in Fig. 3). The fittings yield $C_0 = 2.379$ km s^{-1}, $s_1 = 2.650$ and $s_2 = -3.199$ for the quadratic fitting, and $C_0 = 2.472$ km s^{-1}, and $s = 1.430$ for the linear fitting.

Since index of refraction varies in the shock region for different impact velocities, an additional shift in frequency is added to the probe light, and what DPS actually measures is the apparent velocity u_a. Figure 4 shows the $u_p - u_a$ relation of the 11 Hugoniot shots. u_p and u_a follows a well-defined linear relation for all the impact velocities. Because $u_a \rightarrow u_p$ at small impact velocities, we fit the data with $u_p = ku_a$, and the fitting yields $k = 1.0722(20)$.

For a well-defined shock plateau, the apparent particle velocity can be related to the real particle velocity u_p via [36,37]

$$u_a = n_H u_p + (n_0 - n_H)u_s, \tag{1}$$

where n_0 and n_H are the refractive indices at ambient conditions and a shock state, respectively. n_H can be calculated from Eq. (1) given u_p, u_a, u_s and n_0. Since u_p, u_a, and u_s are accurately measured with the optical beam block system and DPS, the high accuracy of refractive index n_H is guaranteed accordingly. The calculated n_H values are shown as a function of relative density ρ/ρ_0 in Fig. 5. Here, ρ_0 and ρ refer to densities at the unshocked and shocked states, respectively, and the density at shock state can be calculated from the Rankine-Hugoniot jump condition [38, 39],

$$\rho \Big/ \rho_0 = \frac{u_s}{u_s - u_p}. \tag{2}$$

n_H and ρ/ρ_0 follows a linear relation (Fig. 5),

$$n_H = 0.9292(43) + 0.6180(39)\rho/\rho_0, \tag{3}$$

where the fitting uncertainties are indicated by the numbers in the parentheses. $n_H = 1.5472$ is obtained at $\rho/\rho_0 = 1$ according to Eq. (2), showing an excellent agreement with $n_0 = 1.5476$ measured independently at ambient conditions. We also examine the integrated form of the Gladstone-Dale relation [40], i.e., $(n-1)/\rho = \text{constant}$, against our experimental data. The Gladstone-Dale relation slightly underestimates the index of refraction of PET (by $\sim$0.84% for the strongest shot). For
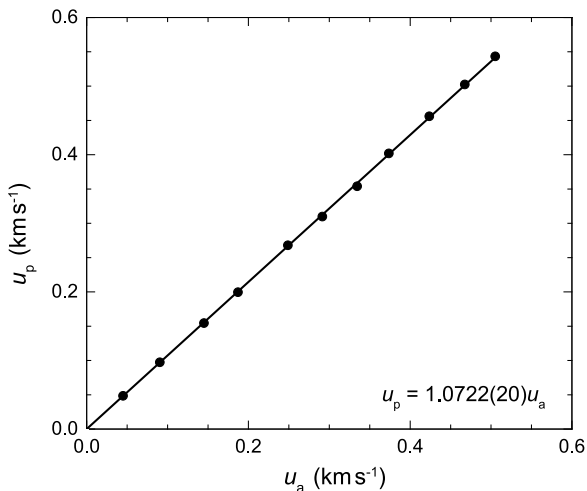

Fig. 5. Refractive index (n_H) as a function of relative density (ρ/ρ_0) at 1550 nm. The black line and red dashed line denote linear fitting and the integrated form of the Gladstone-Dale relation, respectively.

most materials, the index of refraction increases with increasing temperature at a constant density [41,42]. However, the temperature rise induced by shock compression is not considered in Gladstone-Dale relation, thus inducing an underestimation in the index of refraction for PET. The reflecting light from the impact surface becomes rather weak for shot MP675 (the strongest shot, $\sigma_H = 2.362$ GPa), indicating PET can only maintain its transparency below about 2.5 GPa under shock loading.

3.2. Spallation experiments

We conduct 15 spallation shots in total, and some representative free surface velocity histories [$u_{fs}(t)$] are presented in Fig. 6. The curve labelled with A–E describes the wave propagation during plate impact loading, i.e., dynamic shock compression, followed by release and spallation. Segments AB indicate the shock arrival at the sample rear free surface, and BC stands for a supported, stable shock compression state. u_{fs} begins to decrease (CD) as the rarefaction wave initiated from the back surface of the flyer (the sabot recess) arrives at the sample free surface. This rarefaction wave interacts with the one originated from the target rear surface, and then releases the target to tension. Spallation occurs when the tensile stress becomes greater than the critical tensile

Fig. 4. $u_p - u_a$ plot for PET. The solid line denotes fitting with $u_p = ku_a$, where k is a parameter. Error bars are within the symbol size.
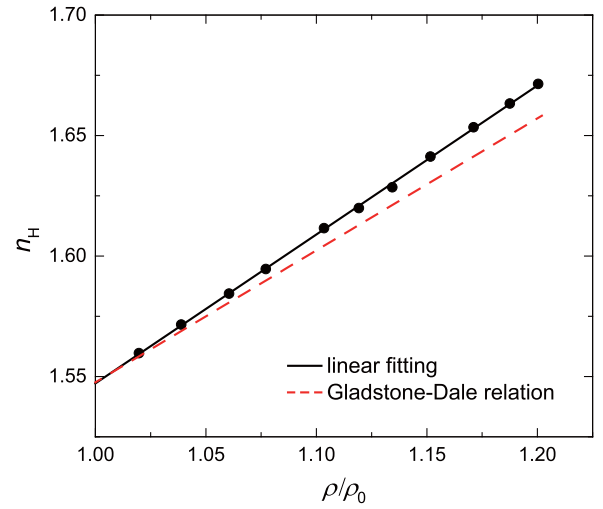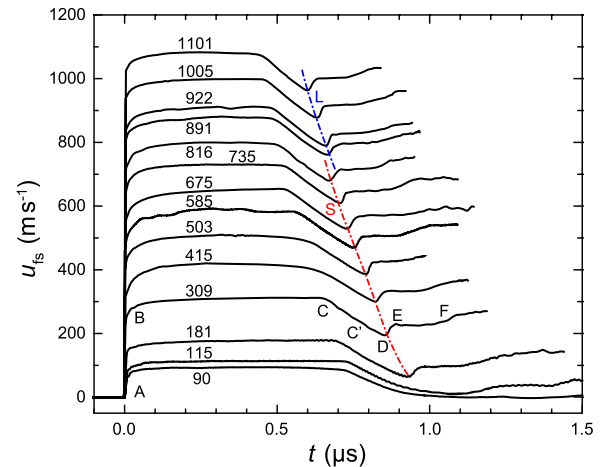

Fig. 6. Free surface velocity u_{fs} time histories of sample for typical spallation shots. Numbers stand for impact velocities of flyer plate in m s^{-1}.

Table 2

Experimental data and parameters for the spallation experiments. h_s: sample thickness; h_f: thickness of flyer plate; u_{imp}: impact velocity; σ_{sp}: spall strength; σ_H: peak stress; $\dot{\varepsilon}$: tensile strain rate; a_r: re-acceleration. The uncertainties is indicated by the numbers in the parentheses for the last one, two, or three digits. "–" in MP712 indicate that no obvious spallation signal is observed in the corresponding free surface velocity history.

Shot number	h_s (mm)	h_f (mm)	u_{imp} (km s^{-1})	σ_{sp} (GPa)	σ_H (GPa)	$\dot{\varepsilon}$ (10^5 s^{-1})	a_r (10^6 s^{-2})
MP712	1.946 (2)	0.980 (2)	0.90 (1)	–	0.150 (3)	–	–
MP687	1.946 (2)	0.955 (2)	0.115 (1)	0.151 (3)	0.194 (3)	0.246 (74)	191 (11)
MP715	1.938 (2)	0.955 (2)	0.155 (1)	0.155 (3)	0.265 (3)	0.606 (55)	451 (22)
MP680	1.948 (2)	0.954 (2)	0.181 (1)	0.167 (3)	0.313 (3)	1.149 (83)	1005 (61)
MP689	1.941 (2)	0.955 (2)	0.309 (2)	0.169 (3)	0.559 (4)	1.334 (84)	1221 (63)
MP692	1.945 (2)	0.960 (2)	0.415 (2)	0.166 (3)	0.773 (5)	1.247 (91)	1263 (87)
MP682	1.945 (2)	0.960 (2)	0.503 (3)	0.168 (3)	0.955 (5)	1.253 (115)	2275 (200)
MP695	1.937 (2)	0.952 (2)	0.585 (3)	0.168 (3)	1.129 (6)	1.357 (76)	1535 (100)
MP696	1.940 (2)	0.961 (2)	0.675 (3)	0.180 (3)	1.331 (6)	1.364 (77)	1551 (119)
MP683	1.938 (2)	0.965 (2)	0.735 (4)	0.171 (3)	1.471 (7)	1.333 (115)	1938 (156)
MP699	1.945 (2)	0.970 (2)	0.816 (4)	0.171 (3)	1.663 (7)	1.515 (118)	1196 (63)
MP704	1.949 (2)	0.979 (2)	0.891 (4)	0.167 (3)	1.849 (8)	1.468 (87)	1484 (144)
MP706	1.941 (2)	0.975 (2)	0.922 (5)	0.176 (3)	1.927 (8)	1.432 (96)	2188 (194)
MP708	1.941 (2)	0.975 (2)	1.005 (5)	0.176 (3)	2.140 (9)	1.692 (85)	2012 (145)
MP709	1.945 (2)	0.961 (2)	1.101 (6)	0.168 (3)	2.395 (10)	1.476 (129)	1586 (112)

strength of sample. A compression wave is generated from spall surface, and induces the subsequent increase in u_{fs} (DE and EF) when the wave reaches the target free surface. The re-acceleration starting at D in $u_{fs}(t)$ is a typical signal for spallation. The slopes of DE and EF depend on independent growth and coalescence of isolated voids or cracks [43,44], respectively.

Mechanical properties such as tensile strain rate ($\dot{\varepsilon}$) and spall strength (σ_{sp}) can be deduced from a free surface velocity history. With the acoustic method, spall strength can be derived from the pullback velocity as [45–49]

$$\sigma_{sp} \approx \rho_0 C_L \Delta u \frac{1}{1 + \frac{C_L}{C_B}}, \tag{4}$$

where $\Delta u = u_{fs,C} - u_{fs,D}$ is the pullback velocity, and C_L and C_B are longitudinal sound velocity and bulk sound velocity, respectively. During release, the tensile strain rate close to spallation (C'D in Fig. 6) is determined with [50,51]

$$\dot{\varepsilon} \approx \frac{1}{2C_B} \frac{du_{fs}(t)}{dt}\Big|_{release}. \tag{5}$$

We use the mean value of $\dot{\varepsilon}$ near spallation in the following discussions. The re-acceleration (DE), a_r, which reflects the failure rate of the sample during spallation [52], can be estimated with

$$a_r = \frac{du_{fs}(t)}{dt}\Big|_{DE}. \tag{6}$$

As indicated in Fig. 6, clear spallation (pullback) signals are observed in the free surface velocity time histories for $u_{imp} > 90$ m s^{-1}, while no spallation signal is found for $u_{imp} = 90$ m s^{-1} under the DPS measurement with a velocity resolution smaller than 1 m s^{-1}. However, the CT characterization reveals minor damage in the sample, which cannot generate a strong enough signature on the free surface velocity history (see below).

Local longitudinal sound speed (for the rarefaction wave initiated from flyer) increases with increasing u_{imp}, so the time of pullback moves towards the left on the free surface velocity curves. The red line "S" in Fig. 6 indicates that the path of the pullback keeps the same trend for $u_{imp} \leq 816$ m s^{-1}. Nevertheless, the pullback shifts toward the right when u_{imp} increases from 816 to 891 m s^{-1}. This reversal is attributed to the sudden drop in local sound velocity, which is induced by release melting.

Table 2 presents the peak shock stress, impact velocity, tensile strain rate, and spall strength as well as other experimental data. In addition, tensile strain rate and spall strength are also depicted as a functions of peak shock stress in Fig. 7(a)–(b). σ_{sp} and $\dot{\varepsilon}$ both increase slightly with increasing σ_H. Furthermore, σ_{sp} also increases slightly with increasing $\dot{\varepsilon}$ as a result of strain-rate-hardening effect [Fig. 7(c)] [53].

3.3. Void characterization

The microstructure induced by spallation in postmortem specimens is examined with CT. CT characterization is only applied to the central part of a postmortem sample to minimize the effects of lateral release on spall damage. The dimensions of a CT sample are $0.66 \times 0.56 \times 1.73$ mm^3 [Fig. 8(a)]. We conduct CT characterization for four shots
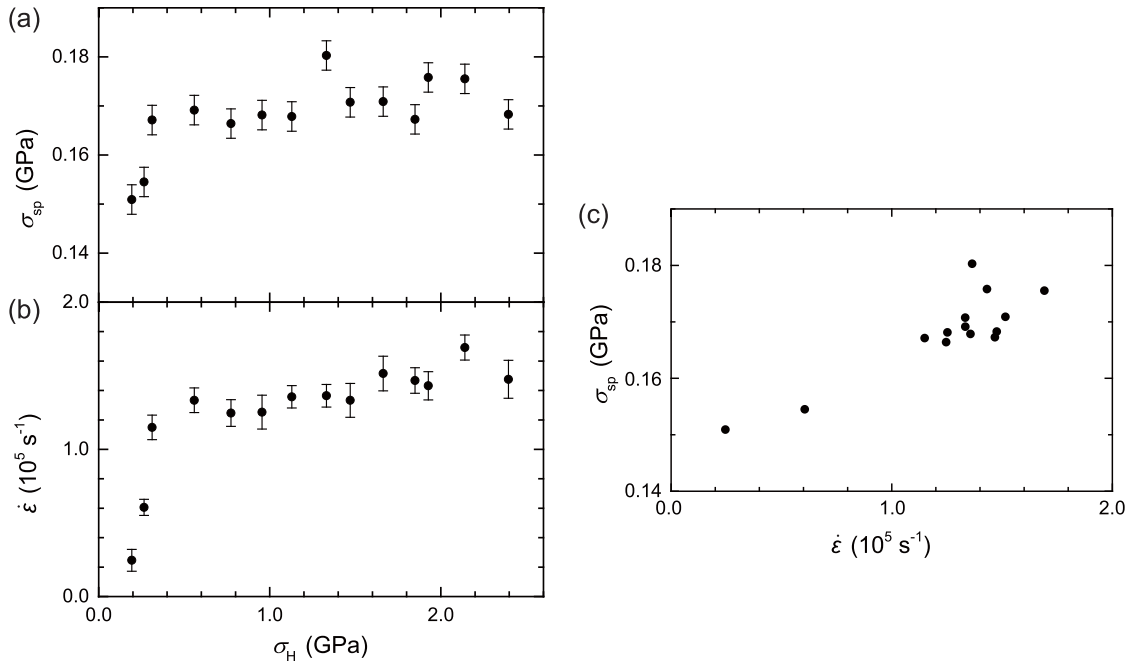

Fig. 7. Experimental results of (a) spall strength and (b) tensile strain rate at different peak shock stresses. (c) Spall strength as a function of tensile strain rate.
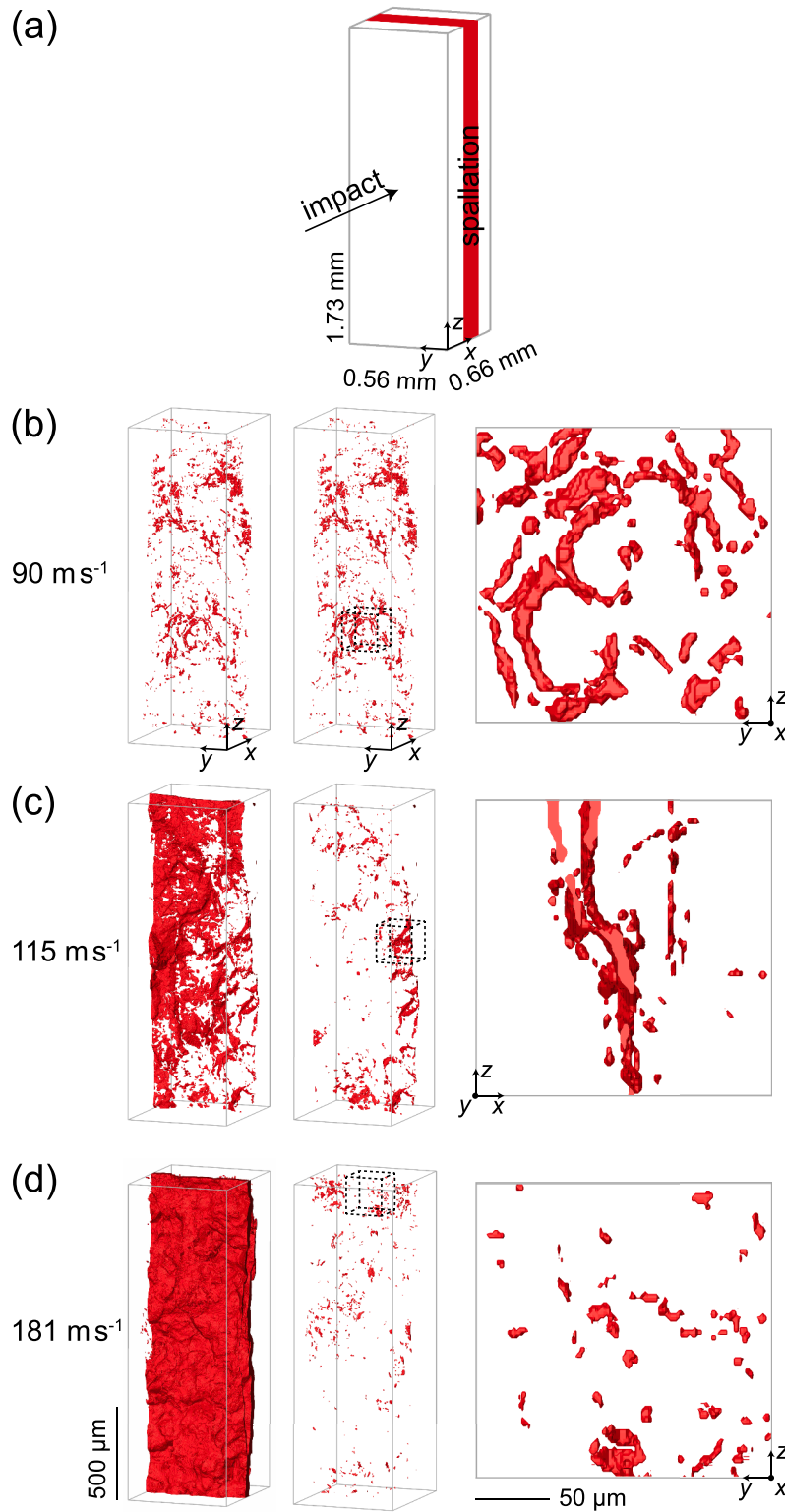
Fig. 8. (a) Dimensions of a CT specimen harvested from a postmortem sample. (b)–(d) CT images of the recovered specimens at different impact velocities as noted. Only voids smaller than 6.5×10^4 μm^3 are shown in the second column. The third column shows enlarged views of the regions indicated with the dashed boxes.

with incipient or full spallation, and some pertinent 3D configurations of microcracks or microvoids are displayed in Figs. 8(b)–(d). When u_{imp} exceeds 200 m s^{-1}, the loaded specimens break into pieces, and cannot be recovered for CT characterizations.

The void shape differs between different impact velocities (Fig. 8). The voids are ellipsoidal and isotropic for the high-speed shot [Fig. 8(d),

181 m s^{-1}], while curved and oriented perpendicular to the impact direction for the low-speed shot [$u_{imp} = 90$ m s^{-1}, Fig. 8(b)]. The ellipsoid-like voids in the high-speed shot are quite common for various materials, including metals and polymers [44,54–56]. Similar to other polymers, there exist stronger covalent bonds between intramolecular atoms, and weaker van der Waals interactions between intermolecular atoms in

PET. For low-speed experiments, the tensile stress induced by rarefaction waves is strong enough to surmount the intermolecular forces (van der Waals force), creating curved and elongated voids between different molecular chains. Nonetheless, the stronger covalent bonds impede further damage process, resulting in elongated voids between different molecules. On the contrary, the intramolecular covalent bonds are broken by the high tensile stress in high-speed shots, leading to ellipsoid-like voids.

Voids initially grow in the yz-plane independently for low-speed shots. During growth of different voids, their stress fields interact with each other; the voids grow toward each other and finally merge. Consequently, curved cracks form as a result of the coalescence process of voids. As two voids on different yz-planes approach each other, their stress fields attract, and the cracks evolve into an oblique crack [Fig. 8 (c)] as a result. The oblique cracks indicate that PET exhibits brittle-type fracture under high strain rates, which is notably different from the ductile-type fracture under low strain rates. With the increase in impact velocity, voids also grow along the loading direction (the x-axis) besides on the yz-plane. As a result, the oblique crack is relatively uncommon in the high-speed shots.

The normalized number density (d_n) of voids is calculated via binning analysis [10,18],i.e.,

$$d_n(i) = \frac{N_{V_j \in [a,b)}}{(b-a)N},\qquad(7)$$

where $d_n(i)$ denotes the normalized number density of the ith volume bin, N refers to the total number of voids, and V_j stands for the volume of the jth void. a and b are chosen to begin with minimal recognizable voids and yield appropriate plotting intervals: $a = 10^{0.421+0.352i}\mu m^3$ and $b = 10^{0.421+0.352(i+1)}\mu m^3$. $[a,b)$ stands for the volume of the ith bin. Fig. 9 displays the d_n values for two representative shots, MP712 and MP715. Due to the difference in void growth mechanisms, d_n of small voids decreases but that of big voids increases with ascending u_{imp} for both shots. As stated above, the tensile stress can only overcome the weaker intermolecular force for low-speed shots, and the intramolecular covalent bonds are retained as a result. Under this circumstance, large amount of small void nuclei is generated because the tensile stress is maintained for a relatively long period. Nevertheless, the covalent bonds are broken rapidly by the intense tension under high-speed impact. Due to the rapid development of damage, the tensile stress only lasts shortly and thus only a small amount of void nuclei are produced, leading to more severe damage and the increased normalized number density of large voids.

To reveal the damage at different positions, we define damage extent as the volume ratio of the concerned damage to the sample under consideration. The damage extent profiles along the impact direction are
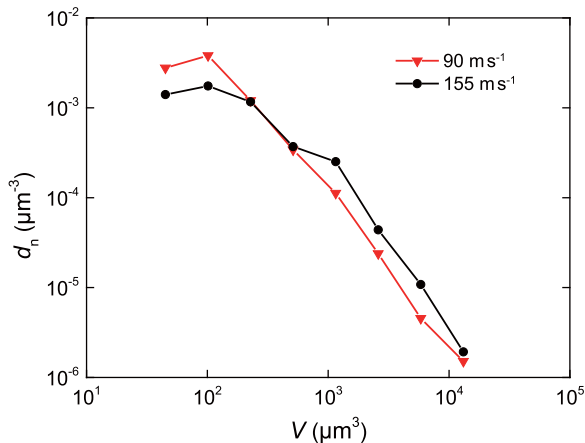

Fig. 9. Void size distribution for MP712 and MP715.
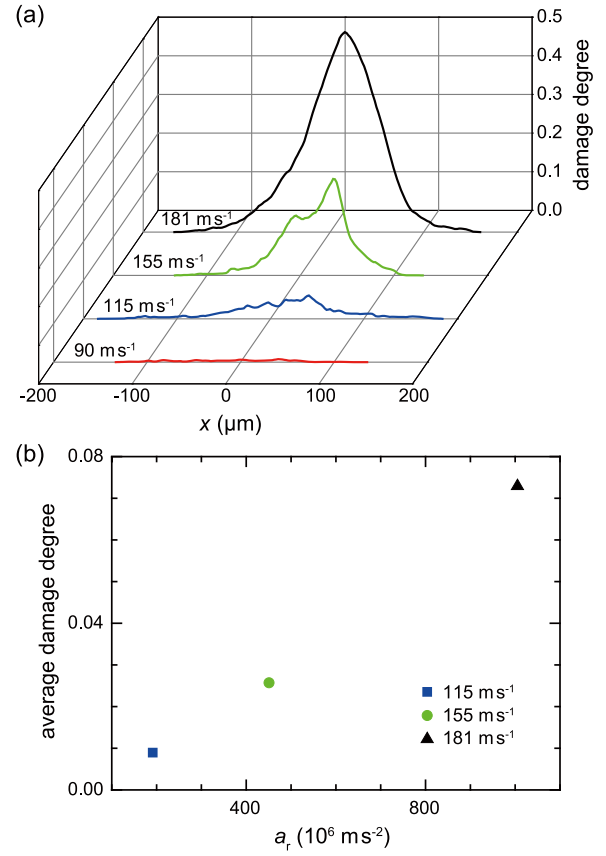

Fig. 10. (a) Damage extent profiles along the loading direction (x-axis) at different loading velocities. The center of a spallation zone is set at $x = 0$. (b) Average damage degree vs re-acceleration for different impact velocities.

depicted for different u_{imp} in Fig. 10(a). With the increase of impact velocity, the damage extent increases significantly while the width of damage region increases slightly. Even though larger tensile stress can accelerate the nucleation and growth of voids for high-speed shots, the shorter period of tensile stress limits its expansion along the loading direction, and the width of the spallation region is almost the same for the lower shock stress cases. Fig. 10(b) presents the relationship between re-acceleration and average damage degree under different impact velocities. A larger a_r indicates faster nucleation and growth of voids, leading to more severe damage in the sample.

4. Conclusions

Free surface velocities are measured for polyethylene terephthalate during planar impact, and CT characterizations are performed on postmortem samples. Impact properties including the Hugoniot equation of state, the relation between apparent velocity and real particle velocity, the refractive indices at shock states, tensile strain rate and spall strength are obtained, along with 3D void configurations of the recovered specimens. The main conclusions are listed as follows.

- The $u_s - u_p$ relation shows a quadratic regime (for $u_p < 250$ m s^{-1}) and a linear regime (for $250 < u_p < 540$ m s^{-1}). The nonlinear relation at low impact velocities may due to plastic yielding and the intermolecular/interchain forces. The index of refraction and relative density at shock states follow a linear relation. PET may only maintain transparency below about 2.5 GPa under shock loading.
- Both tensile strain rate and spall strength slightly increase with increasing peak shock stress after incipient spallation.

- The shape of small voids differs at different impact velocities: ellipsoidal for high-speed experiments but thin and curved for low-speed experiments. The different void shapes may due to the difference in damage mechanisms at different loading velocities, i.e., interchain fracture vs intrachain breakage.

Data availability

The data that support the findings of this study are available upon reasonable request from the authors.

CRediT authorship contribution statement

Y.L. Bian: Conceptualization, Investigation, Visualization, Data curation, Writing – original draft. **H.W. Chai:** Methodology, Visualization. **S.J. Ye:** Investigation, Validation. **H.L. Xie:** Resources. **X.H. Yao:** Supervision, Resources. **Y. Cai:** Validation, Supervision, Writing – review & editing, Project administration, Funding acquisition, Resources.

Declaration of Competing Interest

The authors declare that they have no known competing financial interests or personal relationships that could have appeared to influence the work reported in this paper.

Acknowledgments

References

[1] Davis CH, Mathias LJ, Gilman JW, Schiraldi DA, Shields JR, Trulove P, et al. Effects of melt-processing conditions on the quality of poly (ethylene terephthalate) montmorillonite clay nanocomposites. J Polym Sci Part B 2002;40(23):2661–6.

[2] Rajeev RS, Harkin-Jones E, Soon K, McNally T, Menary G, Armstrong CG, Martin PJ. Studies on the effect of equi-biaxial stretching on the exfoliation of nanoclays in polyethylene terephthalate. Eur Polym J 2009;45(2):332–40.

[3] Bai YL, Yan ZW, Ozbakkaloglu T, Han Q, Dai JG, Zhu DJ. Quasi-static and dynamic tensile properties of large-rupture-strain (LRS) polyethylene terephthalate fiber bundle. Constr Build Mater 2020;232:117241.

[4] Pegoretti A, Kolarik J, Slouf M. Phase structure and tensile creep of recycled poly (ethylene terephthalate)/short glass fibers/impact modifier ternary composites. Express Polym Lett 2009;3(4):235–44.

[5] Cai J, Zhang Q, Chen J, Jiang J, Mo X, He C, Zhao J. Electrodeposition of calcium phosphate onto polyethylene terephthalate artificial ligament enhances graft-bone integration after anterior cruciate ligament reconstruction. Bioact Mater 2021;6(3):783–93.

[6] Martinez AB, Arencon D, Navas J, Velasco JI. Low energy impact indentation of a modified polyethylene terephtalate by instrumented falling weight. J Appl Polym Sci 2013;127(4):2983–9.

[7] Bragov AM, Lomunov AK. Mechanical properties of some polymers and composites at Strain Rates of 1000/s. J Phys IV France 1994;4(C8):C8–337.

[8] Barbosa CN, Gonçalves F, Viana JC. Nano and hybrid composites based on poly (ethylene terephthalate): blending and characterization. Adv Polym Technol 2014;33(2).

[9] Inuwa IM, Arjmandi R, Ibrahim AN, Haafiz MKM, Wong SL, Majeed K, Hassan A. Enhanced mechanical and thermal properties of hybrid graphene nanoplatelets/multiwall carbon nanotubes reinforced polyethylene terephthalate nanocomposites. Fibers Polym 2016;17(10):1657–66.

[10] Curran DR, Shockey DA, Seaman L. Dynamic fracture criteria for a polycarbonate. J Appl Phys 1973;44(9):4025–38.

[11] Saadatfar M, Mukherjee M, Madadi M, Schröder-Turk GE, Garcia-Moreno F, Schaller FM, Hutzler S, Sheppard AP, Banhart J, Ramamurty U. Structure and deformation correlation of closed-cell aluminium foam subject to uniaxial compression. Acta Mater 2012;60(8):3604–15.

[12] Patterson BM, Cordes NL, Henderson K, Williams JJ, Stannard T, Singh SS, et al. In situ X-ray synchrotron tomographic imaging during the compression of hyper-elastic polymeric materials. J Mater Sci 2016;51(1):171–87.

[13] Roth CC, Morgeneyer TF, Cheng Y, Helfen L, Mohr D. Ductile damage mechanism under shear-dominated loading: in-situ tomography experiments on dual phase steel and localization analysis. Int J Plast 2018;109:169–92.

[14] Guessasma S, Belhabib S, Nouri H. Printability and tensile performance of 3D printed polyethylene terephthalate glycol using fused deposition modelling. Polymers 2019;11(7):1220.

[15] Lu ZH, Liu HJ, Wei PT, Zhu CC, Xin D, Shen YQ. The effect of injection molding lunker defect on the durability performance of polymer gears. Int J Mech Sci 2020;180:105665.

[16] Liao BB, Zhou JW, Ai SG, Lin Y, Xi L, Cao Y, et al. Comparison of laminate thickness on the low velocity impact behaviors for Z-pinned composite laminates. Int J Mech Sci 2021:106567.

[17] Verker R, Eliaz N, Gouzman I, Eliezer S, Fraenkel M, Maman S, Beckmann F, Pranzas K, Grossman E. The effect of simulated hypervelocity space debris on polymers. Acta Mater 2004;52(19):5539–49.

[18] Ye SJ, Chai HW, Xiao XH, Cai Y, Yao XH, Luo SN. Spallation of polycarbonate under plate impact loading. J Appl Phys 2019;126(8):085105.

[19] Barker LM, Hollenbach RE. Shock-wave studies of PMMA, fused silica, and sapphire. J Appl Phys 1970;41(10):4208–26.

[20] Chapman DJ, Eakins DE, Williamson DM, Proud W. Index of refraction measurements and window corrections for PMMA under shock compression. AIP Conf. Proc. vol. 1426. American Institute of Physics; 2012. p. 442–5.

[21] Turneaure SJ, Sinclair N, Gupta YM. Real-time examination of atomistic mechanisms during shock-induced structural transformation in silicon. Phys Rev Lett 2016;117(4):045502.

[22] Pélissier JL, Partouche-Sebban D. Pyrometry measurements on shock-heated bismuth using PMMA and sapphire windows. Phys B 2005;364(1–4):14–28.

[23] Iiyama K, Ishida T, Ono Y, Maruyama T, Yamagishi T. Fabrication and characterization of amorphous polyethylene terephthalate optical waveguides. IEEE Photon Technol Lett 2011;23(5):275–7.

[24] Gustavsen RL, Sheffield SA, Alcon RR, Medina RS. Changes to the LANL gas driven two stage gun: projectile velocity measurement and etc. Tech. Rep. Los Alamos Natl. Lab.; 2001.

[25] Li XJ, Li B, Liu QH. Design and application of velocity measuring system for the flying projectiles base on the laser. 2010 International conference on computer, mechatronics, control and electronic engineering. vol. 3. IEEE; 2010. p. 84–7.

[26] Strand OT, Goosman DR, Martinez C, Whitworth TL, Kuhlow WW. Compact system for high-speed velocimetry using heterodyne techniques. Rev Sci Instrum 2006;77(8):083108.

[27] DeCarli PS, Meyers MA. Design of uniaxial strain shock recovery experiments. Shock waves high-strain-rate Phenom. Met. Springer; 1981. p. 341–73.

[28] Williams CL. Structure-property relationships under extreme dynamic environments: shock recovery experiments. Synth SEM Lect Exp Mech 2019;2(1):1–155.

[29] Tan J, Lu L, Li HY, Xiao XH, Li Z, Luo SN. Anisotropic deformation and damage of dual-phase Ti-6Al-4V under high strain rate loading. Mater Sci Eng A 2019;742:532–9.

[30] Chai HW, Xie ZL, Xiao XH, Xie HL, Huang JY, Luo SN. Microstructural characterization and constitutive modeling of deformation of closed-cell foams based on in situ x-ray tomography. Int J Plast 2020;131:102730.

[31] Gürsoy D, Carlo FD, Xiao X, Jacobsen C. TomoPy: a framework for the analysis of synchrotron tomographic data. J Synchrotron Radiat 2014;21(5):1188–93.

[32] Carter WJ, Marsh SP. Hugoniot equation of state of polymers. Tech. Rep. Los Alamos National Lab., NM (United States); 1995.

[33] Johnson JN, Dick JJ, Hixson RS. Transient impact response of three polymers. J Appl Phys 1998;84(5):2520–9.

[34] Bourne NK, Millett JCF, Brown EN, Gray III GT. Effect of halogenation on the shock properties of semicrystalline thermoplastics. J Appl Phys 2007;102(6):063510.

[35] Bourne NK, Millett JCF. On the influence of chain morphology on the shock response of three thermoplastics. Metall Mater Trans A 2008;39(2):266–71.

[36] Huang JW, Liu QC, Zeng XL, Zhou XM, Luo SN. Refractive indices of Gd$_3$Ga$_5$O$_{12}$ single crystals under shock compression to 100–290 GPa. J Appl Phys 2015;118(20):205902.

[37] Li Y, Zhou XM, Liu CL, Luo SN. Refractive indices of CaF$_2$ single crystals under elastic shock loading. J Appl Phys 2017;122(4):045901.

[38] Duvall GE, Graham RA. Phase transitions under shock-wave loading. Rev Mod Phys 1977;49(3):523.

[39] Rigg PA, Knudson MD, Scharff RJ, Hixson RS. Determining the refractive index of shocked [100] lithium fluoride to the limit of transmissibility. J Appl Phys 2014;116(3):033515.

[40] Wise JL, Chhabildas LC. Laser interferometer measurements of refractive index in shock-compressed materials. Shock waves condens. Matter. Springer; 1986. p. 441–54.

[41] Waxler RM, Cleek G. The effect of temperature and pressure on the refractive index of some oxide glasses. J Res Natl Bur Stand A Phys Chem 1973;77(6):755.

[42] Kasarova SN, Sultanova NG, Nikolov ID. Temperature dependence of refractive characteristics of optical plastics. J Phys Conf Ser 2010;253:012028.

[43] Zurek AK, Thissell WR, Johnson JN, Tonks DL, Hixson R. Micromechanics of spall and damage in tantalum. J Mater Process Tech 1996;60(1–4):261–7.

[44] Li C, Li B, Huang JY, Ma HH, Zhu J, Luo SN. Spall damage of a mild carbon steel: effects of peak stress, strain rate and pulse duration. Mater Sci Eng A 2016;660:139–47.

[45] Stepanov GV. Spall fracture of metals by elastic-plastic loading waves. Probl Prochn 1976;8:66–70.

[46] Antoun T, Seaman L, Curran DR, Kanel GI, Razorenov SV, Utkin AV. Spall fracture. Springer Science & Business Media; 2003.

[47] Kanel GI. Spall fracture: methodological aspects, mechanisms and governing factors. Int J Fract 2010;163(1–2):173–91.

[48] Cai Y, Wu HA, Luo SN. Spall strength of liquid copper and accuracy of the acoustic method. J Appl Phys 2017;121(10):105901.

[49] Fernando PLN, Mohotti D, Remennikov A, Hazell PJ, Wang H, Amin A. Experimental, numerical and analytical study on the shock wave propagation through impedance-graded multi-metallic systems. Int J Mech Sci 2020;178: 105621.

[50] Luo SN, An Q, Germann TC, Han LB. Shock-induced spall in solid and liquid Cu at extreme strain rates. J Appl Phys 2009;106(1):013502.

[51] Arman B, Luo SN, Germann TC, Çağın T. Dynamic response of $Cu_{46}Zr_{54}$ metallic glass to high-strain-rate shock loading: Plasticity, spall, and atomic-level structures. Phys Rev B 2010;81(14):144201.

[52] Kanel GI, Utkin AV. Estimation of the spall fracture kinetics from the free-surface velocity profiles. AIP Conf. Proc. vol. 370. American Institute of Physics; 1996. p. 487–90.

[53] Khan A, Zhang H. Finite deformation of a polymer: experiments and modeling. Int J Plast 2001;17(9):1167–88.

[54] Yao Y, Chai HW, Li C, Bie BX, Xiao XH, Huang JY, Qi ML, Luo SN. Deformation and damage of sintered low-porosity aluminum under planar impact: microstructures and mechanisms. J Mater Sci 2018;53(6):4582–97.

[55] Soulard L, Bontaz-Carion J, Cuq-Lelandais JP. Experimental and numerical study of the tantalum single crystal spallation. Eur Phys J B 2012;85(10):1–15. 332.

[56] Bontaz-Carion J, Pellegrini YP. X-ray microtomography analysis of dynamic damage in tantalum. Adv Eng Mater 2006;8(6):480–6.